SUPPLEMENTARY NOTE FOR:

Actin cortex architecture regulates cell surface tension

Priyamvada Chugh, Andrew G. Clark, Matthew B. Smith, Davide A. D. Cassani, Kai Dierkes, Anan Ragab, Philippe P. Roux, Guillaume Charras, Guillaume Salbreux and Ewa K. Paluch

Contents

Description of cortex simulations.

We introduce three components in our simulations: actin filaments, crosslinkers, and myosin minifilaments (Fig. 4a). A list of the simulations parameters is given in Supplementary Table 5.

Actin filaments are treated as rigid rods (see Discussion of model assumptions below) with a finite length, l_a, ranging between 200 nm and 800 nm for the different simulation conditions. For each simulation, all filaments had the same length (we checked the robustness of our conclusions by introducing a Gaussian distribution in filment length, Supplementary Fig. 5e). The unit vector giving the orientation of filament i is denoted $\mathbf{n}_i$ (Supplementary Fig. 5a), and points towards the plus end of the actin filament.

Myosin minifilaments are simulated as three distinct sections, a "bare zone" and two connecting heads, with a total length of approximately 300 nm (1). The bare zone is simulated as a rigid stalk with a length $l_m = 200$ nm. At both ends of the bare zone, the connecting heads can bind to actin filaments (Supplementary Fig. 5a). The connecting heads are treated as springs with stiffness k_{ms} and reference length of $l_{ms}^0 = 50$ nm, such that the force in the end-spring, f_{ms}, is:

$$f_{ms} = k_{ms} \left(l_{ms} - l_{ms}^0 \right), \tag{1}$$

where l_{ms} is the distance between the end of the bare zone and the point on the actin filament that the connecting head is attached to. The junctions between the minifilament bare zone and either end-spring, as well as junction between the end-springs and actin filament, can freely rotate. The position of attachment for myosin minifilament k on actin filament i is measured as the distance from the center of mass of the actin filament, and is denoted s_{ki} (Supplementary Fig. 5c).

Crosslinkers are treated as short springs that attach to two actin filaments (Fig. 4a). Crosslinkers have a stiffness k_x and a resting length $l_x^0 = 50$ nm, such that the force produced by a crosslinker is defined as:

$$f_x = k_x(l_x - l_x^0), \tag{2}$$

where l_x is the distance between the points of attachment on the actin filaments the crosslinker is attached to.

We simulate the network in three dimensions, x, y, z. We denote the cartesian unit vectors $\mathbf{e}_x$, $\mathbf{e}_y$, $\mathbf{e}_z$ (Supplementary Fig. 5a, b). The boundary conditions in the x and y directions are periodic, with the width, W, equal to 2.5 µm (Supplementary Fig. 5b). There are no boundary conditions in the z direction.

Initialization

The simulation is initialized by placing N_f actin filaments within the simulation box, at random positions along the x and y directions. In the z direction filament positions are limited by the seeding thickness, h_0 (Supplementary Fig. 5b). Their initial z position is placed randomly within the interval $-h_0/2 \leq z \leq h_0/2$ in the z direction. Filament orientations can be written

2

in spherical coordinate:

$$\mathbf{n}_i = (\sin\theta\cos\phi)\,\mathbf{e}_x + (\sin\theta\sin\phi)\,\mathbf{e}_y + (\cos\theta)\,\mathbf{e}_z, \tag{3}$$

where the angles θ and ϕ are taken from the probability distribution

$$P(\theta,\phi) = \frac{\sin\theta}{4\pi\sin\frac{\sigma_a}{2}}\Theta\left(\frac{\theta - \frac{\pi}{2}}{\sigma_a}\right). \tag{4}$$

The function $\Theta(x)$ is 1 for $-\frac{1}{2} < x < \frac{1}{2}$ and is 0 otherwise. $P(\theta)$ is chosen such that filament orientations are uniformly distributed within the limiting angle, σ_a, such that $\frac{\pi}{2} - \frac{\sigma_a}{2} < \theta < \frac{\pi}{2} + \frac{\sigma_a}{2}$. For $\sigma_a = 0$, filaments are parallel to the x,y plane, and for $\sigma_a = \pi$, they are isotropically oriented.

The seeding thickness, h_0, is chosen to keep the mean actin length density, defined as

$$\rho_f = \frac{N_f l_a}{W^2 h_0}, \tag{5}$$

constant for the varying actin lengths. We chose a density that correspond roughly to the density observed using SEM data (Fig. 1g and Supplementary Fig. 2h, i), where about 75% of the surface was covered with actin filaments.

Crosslinkers are introduced in the simulation by looking for possible binding sites where two filaments are separated by a distance less than l_x^0. A crosslinker is then added to each potential binding site with probability p_x. Crosslinkers are added in their resting configuration by attaching one end of the crosslinker to a potential binding site on the first filament and looking for a position at distance l_x^0 on the other filament. If there are two possible sites, one site is chosen randomly.

Finally, myosin minifilaments are placed by positioning one of the end-springs on a randomly chosen actin filament, and searching the remaining actin filaments within a distance l_m for potential binding sites at a distance $l_m + 2l_{ms}^0$. If such a binding site exists, the myosin links the two filaments in a straight, unstretched configuration. If more than one binding site exists, one site is chosen at random, and when no filaments satisfy the condition, the second end is left free and placed randomly.

Dynamics

After initialization, the simulation runs in two phases. In the first phase, myosin minifilaments bind and unbind actin filaments, or minifilaments that are bound to an actin filament can walk towards the plus end of actin filaments. In the second phase, after every step of myosin interaction, the network is relaxed quasi-statically until a criterion defined below is met.

Myosin binding and walking dynamics

Myosins can unbind actin filaments because they reach the end of the filament or because they spontaneously unbind. Spontaneous unbinding occurs randomly with a mean lifetime of τ_m.

When a minifilament head binds to an actin filament, a lifetime is chosen from an exponential distribution with mean τ_m. If the amount of time the minifilament has remained bound exceeds the chosen lifetime, the head unbinds. When both heads of a myosin minifilament are free, the myosin minifilament immediately rebinds a filament in the network at a random location, following the same procedure used during initialization. As a result, the number of myosins bound in the network is fixed.

At every step, the binding position of myosin minifilament k on filament i, denoted s_{ki}, is updated according to the following equation:

$$\alpha_s \frac{ds_{ki}}{dt} = f_0 + \mathbf{f}_{ms} \cdot \mathbf{n}_i, \tag{6}$$

where α_s is an effective friction coefficient between the motor and the filament, the stall force, f_0, is an active force that is generated by the minifilament towards the plus end of the actin filament, and $\mathbf{f}_{ms}$ is oriented from the point of attachment towards the end of the minifilament and has a magnitude set by Eq. 1. When the projection along the direction of the filament of the tension in the end-spring is equal to $-f_0$, the head does not move (Supplementary Fig. 5c).

Network relaxation

After myosin binding has been updated, the network is relaxed quasi-statically, without updating myosin positions on actin filaments. Below, we denote t^* as a fictitious time coordinate used for this relaxation. Network relaxation is performed for both actin filaments and myosin minifilaments. The centers of mass, $\mathbf{r}_i$, and orientations, $\mathbf{n}_i$, are updated according to the following equations:

$$\alpha_t \frac{d\mathbf{r}_i}{dt^*} = \sum_k \mathbf{f}_{ik} \tag{7}$$

$$\alpha_r \frac{d\mathbf{n}_i}{dt^*} = -\mathbf{n}_i \times \left(\sum_k s_k \mathbf{n}_i \times \mathbf{f}_{ik} \right), \tag{8}$$

where $\mathbf{f}_{ik}$ is the force acting on filament i by a spring-like attachment k (crosslinker or myosin head binding). α_t and α_r are translational and rotational fictitious friction coefficients. Steric interactions are not considered, which means filaments and crosslinkers only interact if they are bound. As a result filaments, crosslinkers, and myosins can freely pass through each other.

Iteration is performed by discretising equations 7 and 8 with an Euler explicit scheme with adaptive steps. The network relaxation is performed for 10000 trial steps, or if the following criterion is satisfied. The norms of the total force and torque for each filament

$$\mathbf{f}_i = \sum_k \mathbf{f}_{ik} \tag{9}$$

$$\tau_i = \sum_k s_k \mathbf{n}_i \times \mathbf{f}_{ik} \tag{10}$$

are averaged over all actin filaments and myosin minifilaments i to obtain:

$$e = \frac{1}{N} \left[\sum_i \frac{|\mathbf{f}_i|}{f_0} + \sum_i \frac{|\tau_i|}{f_0 l_0} \right] \tag{11}$$

4

where N is the total number of actin and myosin filaments, and l_0 is a reference length set to 250 nm. The relaxation is stopped when e is less than the relaxation limit parameter e_{max} (Supplementary Table 5) and $\max(|\mathbf{f}_i|/f_0) < 0.01$.

Network surface tension measurement

The network surface tension T is measured by slicing the network with a plane and calculating the total force F acting normal to the plane (Fig. 4a). The total force F is obtained by summing the forces acting within actin filaments, myosin minifilaments and crosslinkers cut by the plane (Supplementary Fig. 5d). The surface tension is then calculated according to:

$$T = \frac{F}{W} \tag{12}$$

In practice the tension is measured by slicing with two different planes, the plane perpendicular to the x-axis to measure T_x, and the plane perpendicular to the y-axis to measure T_y, both going across the center of the simulation box. The network is further relaxed to equilibrium prior to tension measurement. We then report the average surface tension $(T_x + T_y)/2$.

In Figures 4c, d, 5a and Supplementary Figure 5e-g, we also normalize the surface tension to a reference surface tension T_0 defined as:

$$T_0 = \frac{f_0 \left(l_m + 2l_{ms}^0\right) N_m}{W^2}, \tag{13}$$

which is the product of the characteristic myosin force dipole, $f_0(l_m + 2l_{ms}^0)$, and the two-dimensional concentration of myosins, N_m/W^2. For our choice of parameters, $T_0 \simeq 230$ pN/μm.

To obtain the average tensions plotted in Figs. 4d, 5a and Supplementary Fig. 5e-g, we average the tension between $t_0 = 25$ s and the total simulation time $t = 200$ s.

Local strain and network stress measurement

We now describe the calculation of strain from simulations of deformed actin networks (Fig. 5). We used projected views of the 3D network on a 2D plane. A square lattice is defined with side length $l_l/W = 0.02$. For each point in the lattice, a neighbourhood region is defined as the circle with radius $l_l/4$ centered around the lattice point. For each lattice point, only filaments located within the neighbourhood are taken into account. The set of positions of points on these filaments that are closest to the lattice point is then obtained in the initial state, $\{\mathbf{P}_i\}$ and deformed state, $\{\mathbf{P}_f\}$. The initial position of lattice point is repositioned to the average of the points within the neighbourhood, $\langle\{\mathbf{P}_i\}\rangle$. The deformation vector of each lattice point is obtained from $\langle\{\mathbf{P}_f\}\rangle$- $\langle\{\mathbf{P}_i\}\rangle$.

A set of triangles is then obtained by connecting two opposite points within each cell of the lattice. The relative change of area of each triangle under the deformation field is calculated to obtain a field of isotropic strain (Fig. 5b).

To calculate the local 2D network stress, a square lattice is defined with the same side length $l_l/W = 0.02$. The isotropic 2D stress acting in the center of each lattice cell, $(T_{xx} + T_{yy})/2$, is then calculated.

Additional simulations

Variability in filament length

In the actin cortex, filaments may have varying lengths. To test how actin filaments length distribution affects our results, we ran simulations where the filament lengths have a Gaussian distribution with standard deviations of 10%, 20%, and 30% of the mean length. These simulations were run for three different average filament lengths, $l_a = 290$ nm, $l_a = 440$ nm, and $l_a = 620$ nm, which correspond to three regions of tension generation: low tension, peak tension and medium tension respectively (Supplementary Fig. 5e). We find that the network tension increases for short filament networks when the standard deviation of filament length increases, but a peak tension still appears at intermediate filament lengths for all standard deviations tested.

Changing cortex seeding thickness at fixed filament length

We then tested whether the choice of seeding thickness of the simulated cortex alone affects the magnitude of the generated tension. We ran simulations at a fixed actin density, filament length, and number of myosin motors for a range of seeding thickness values ($h_0 = 103$ nm to 412 nm, Supplementary Fig. 5f). The density was fixed by setting the number of filaments to $N_f = \beta h_0$ with $\beta = 11.37$ nm^{-1}, to match the density in the original simulations. All simulations were run with $l_a = 500$ nm. We find that the tension is weakly dependent on the seeding thickness, but does not exhibit a maximum tension at intermediate seeding thicknesses (Supplementary Fig. 5f).

Changing filament length at fixed seeding thickness

We then tested for the effect of filament length on tension generation when the total amount (total length) of actin $L_a = N_f l_a$ and the seeding thickness h_0 are kept constant (Supplementary Fig. 5g). We ran simulations where the filament length was varied over the range 200 nm to 800 nm, similar to the range explored in Fig. 4d. The number of the filaments N_f was set to the closest integer to L_a/l_a with $L_a = 693.75$ μm, the seeding thickness was set to $h_0 = 250$ nm, and the crosslinker binding probability was changed to $p_x = 0.5$, to account for a decrease in actin density relative to the simulations displayed in Fig. 4d. The results show that filament length still modulates tension, with a peak at intermediate filament lengths (Supplementary Fig. 5g).

6

Discussion of model assumptions

We briefly discuss here some of the model assumptions.

Discussion of myosin stall force and kinetics

Myosin minifilaments represent filaments of myosin II motors. Individual myosin II motors have been shown to produce between 2 and 5 pN of force (2). Individual motors are not processive, but have been shown to assemble into minifilaments of 10 to 30 motors *in vitro* (3) and in the lamellipodium of fibroblasts (4). Based on this evidence, it is expected that myosin motors behave collectively as an ensemble of motors (5). In our simulations, we chose for simplicity a linear force-velocity relationship describing the effective behaviour of one mini-filament. We also have set the minifilament stall force to a value of 40 pN, as previously estimated based on the assumption that there are about 20 myosin motors per minifilament, with individual motors producing an average of 2 pN while working in the ensemble (6).

Discussion of the assumption of rigid rods

For simplicity, we took actin filaments to be straight rods in our simulations, assuming that the distance between crosslinkers is sufficiently small or the filament bending rigidity sufficiently high. We discuss here this assumption. Note that calculating the bending of filaments in a crosslinked network is a complex problem and we only intend here to estimate rough orders of magnitudes.

An estimate of the average distance between crosslinkers, d_x, in simulated networks can be obtained by taking the total length of actin and dividing by twice the total number of crosslinkers, N_x:

$$d_x = \frac{N_f l_a}{2 N_x}. \tag{14}$$

The value of d_x calculated from simulations depends on the length of filaments. With filament lengths l_a taken between 200 nm to 800 nm, we take from simulations $N_x \sim 8000$ for the lowest filament length and $N_x \sim 21000$ for the largest filament length, and therefore 30 nm$< d_x <$ 60 nm. This characteristic distance between crosslinking points is small when compared to the persistence length of actin filaments, ~ 10 μm.

To give an order of magnitude of how much filaments could bend if the filament bending rigidity was taken into account, we first calculate the deformation induced by a normal force acting on a portion of filament between two crosslinkers. For simplicity we consider here a filament between two crosslinking points as a simply supported beam of length L, subjected to a force F acting in the middle of the filament. The deflection can then be written:

$$w = \frac{F L^3}{48 \kappa}, \tag{15}$$

where κ is the actin filament flexural rigidity that can be calculated from the actin persistence length $l_p \simeq 10$ μm (11), $\kappa = l_p k_b T \simeq 4.1 \times 10^{-26}$ N m^2. Using L=60 nm a characteristic

distance between crosslinking points and taking $F = f_0 = 40$ pN the force exerted by one myosin minifilament, we calculate a deflection w of about ~ 4 nm, small compared to the length of actin filaments and to the distance between cross linkers (see above).

One can also estimate the buckling threshold for one filament that would result from an axial load along the filament. To consider this we use the Euler buckling equation,

$$F^* = \frac{\pi^2 \kappa}{(KL)^2}. \tag{16}$$

where F^* is the critical applied load tangential to the filament, K is the column effective length factor which depends on boundary conditions applied on the filament and take values between 0.5 and 2, and L is the length at which the beam becomes unstable. Imposing F^* to be equal to the force exerted by one myosin minifilament $f_0 = 40$ pN, we find a critical length L for actin filaments to undergo a buckling instability between 50 nm and 200 nm. Again considering here for simplicity that the filament is fixed at its crosslinking positions, this shows that the largest mean distance between crosslinkers is at the lower limit of buckling lengths, suggesting that buckling under axial loads imposed by myosin minifilaments is unlikely to be a frequent event in our simulations. In general, crosslinkers are not rigidly fixed in a network and the network behaviour thus likely to be more complex than considered here.

While filament bending, in principle, could occur in the actin cortex, our simulations indicate that taking filament bending into account is not necessary to generate tension, as has been shown in previous studies (7, 8). In addition to exhibiting contractility, our simulated actomyosin networks produce a non-monotonic relationship between tension and filament length. Including filament bending in simulations would be interesting but would require imposing a value for the filament bending rigidity, which can be influenced by a number of factors, including: bundling of actin filaments (9), actin binding proteins (e.g. tropomyosin (10), cofilin (11)) or the nucleotide state (ATP or ADP-bound) of monomers in the filaments (12). For all these reasons, we chose not to include bending in our model. Interestingly, several previous studies have proposed that filament bending under compression could be a mechanism accounting for cortical tension generation in actomyosin networks (see Discussion in Main Text and references 13-15). In our model, tension generation is achieved without this effect and results from asymmetries in actin network response to myosin stresses (Fig. 5). It will be interesting in the future, to investigate the influence of filament bending on tension generation in our model.

Additional References

1. Svitkina, T. M., Verkhovsky, A. B., and Borisy, G. G. Improved procedures for electron microscopic visualization of the cytoskeleton of cultured cells. *J. Struct. Biol.* **115**, 290–303 (1995).

2. Finer, J. T., Simmons, R. M., Spudich, J. A., et al. Single myosin molecule mechanics: piconewton forces and nanometre steps. *Nature* **368**(6467), 113–119 (1994).

3. Niederman, R. and Pollard, T. D. Human platelet myosin II. In vitro assembly and structure of myosin filaments. *J. Cell Biol.* **67**(1), 72–92 (1975).

4. Verkhovsky, A. B. and Borisy, G. G. Non-sarcomeric mode of myosin II organization in the fibroblast lamellum. *J. Cell Biol.* **123**(3), 637–652 (1993).

5. Erdmann, T. and Schwarz, U. S. Stochastic force generation by small ensembles of myosin II motors. *Phys. Rev. Lett.* **108**(18), 188101 (2012).

6. Nie, W., Wei, M.-T., Ou-Yang, H. D., Jedlicka, S. S., and Vavylonis, D. Formation of contractile networks and fibers in the medial cell cortex through myosin-II turnover, contraction, and stress-stabilization. *Cytoskeleton* **72**(1), 29–46 (2015).

7. Carlsson, A. E. Contractile stress generation by actomyosin gels. *Phys. Rev. E* **74**(5), 051912 (2006).

8. Hiraiwa, T. and Salbreux, G. Role of turnover in active stress generation in a filament network. *Phys. Rev. Lett.* **116**(18), 188101 (2016).

9. Claessens, M. M. A. E., Bathe, M., Frey, E., and Bausch, A. R. Actin-binding proteins sensitively mediate f-actin bundle stiffness. *Nat. Mater.* **5**(9), 748–753, 09 (2006).

10. Kojima, H., Ishijima, A., and Yanagida, T. Direct measurement of stiffness of single actin filaments with and without tropomyosin by *in vitro* nanomanipulation. *Proc. Natl. Acad. Sci. U.S.A.* **91**(26), 12962–12966 (1994).

11. McCullough, B. R., Blanchoin, L., Martiel, J.-L., and Enrique, M. Cofilin increases the bending flexibility of actin filaments: implications for severing and cell mechanics. *J. Mol. Biol.* **381**(3), 550–558 (2008).

12. Isambert, H., Venier, P., Maggs, A., Fattoum, A., Kassab, R., Pantaloni, D., and Carlier, M. Flexibility of actin filaments derived from thermal fluctuations. effect of bound nucleotide, phalloidin, and muscle regulatory proteins. *J. Biol. Chem.* **270**(19), 11437–11444 (1995).

13. Soares e Silva, M., Depken, M., Stuhrmann, B., Korstena, M., MacKintosh, F. C. Active multistage coarsening of actin networks driven by myosin motors. *Proc. Natl. Acad. Sci. USA* **108**, 9408–9413 (2011).

14. Lenz, M., Thoresen, T., Gardel, M. L. and Dinner, A. R. Contractile units in disordered actomyosin bundles arise from F-actin buckling. *Phys. Rev. Lett.* **108**, 238107 (2012).

15. Murrell, M. P. and Gardel, M. L. F-actin buckling coordinates contractility and severing in a biomimetic actomyosin cortex. *Proc. Natl. Acad. Sci. USA* **109**, 20820–20825 (2012).

16. Clark, A. G. *Thickness, dynamics and mechanics of the actomyosin cortex.* PhD thesis, Technische Universität Dresden, Dresden, Germany, (2013).

17. Machicoane, M., de Frutos, C. A., Fink, J., Rocancourt, M., Lombardi, Y., Garel, S., Piel, M., and Echard, A. Slk-dependent activation of ERMs controls LGN–NuMA localization and spindle orientation. *J. Cell Biol.* **205**(6), 791–799, 06 (2014).

18. Estey, M. P., Di Ciano-Oliveira, C., Froese, C. D., Bejide, M. T., and Trimble, W. S. Distinct roles of septins in cytokinesis: Sept9 mediates midbody abscission. *J. Cell Biol.* **191**(4), 741–749, 11 (2010).

Supplementary legends for "Actin cortex architecture regulates cell surface tension"

Supplementary Figures:

Supplementary Figure 1: Cortex tension measurements using tipless cantilever atomic force microscopy (AFM). (a) Representative YZ image of a mitotic adherent HeLa cell with plasma membrane labelled using CellMask Deep Red[TM] (magenta) and cantilever visualized by laser reflection (green). Scale bar = 5 μm. (b) Schematic of tipless cantilever AFM assay. r_{mid}: radius of the maximum cross sectional area of the cell; r_c: radius of the contact area of the cell with the cantilever; and h_{cell}: height of the cell. (c) AFM force curve from a cell compression experiment. Red arrow indicates the time point after initial force relaxation, at which cell height is recorded. Confocal stack acquisition for cell height recording induces force fluctuations (not displayed), therefore force is measured before the confocal stack is acquired. (d) Calculation of the correction coefficient for refractive index mismatches. Plot of mES cell height values directly measured by AFM vs. those extracted from confocal stacks of mESCs with the membrane labelled (peak-to-peak distance). The slope calculated from linear fitting was used to correct for optical aberrations due to refractive index mismatch in cell height measurements, see Methods for details. Points represent individual measurements (n=30 cells from 3 independent experiments).

Supplementary Figure 2: Extended measurements of cortex properties in interphase and mitosis. (a,b) Full width at half-maximum (FWHM) of membrane linescans (p=0.050, 0.16, 0.025, 0.82) (a) and cell radii (p=9.8x10^{-13}, 7.2x10^{-6}, 0.0062,

0.048) (b) for different cell lines in interphase and mitosis (n=41, 100, 47, 27, 11, 13, 22, 13 individual measurements from 2-13 independent experiments). (c) Cortex thickness measurements for interphase HeLa cells detached using trypsin or enzyme-free detachment (Enz.-Free) and immobilized by centrifugation on Poly-L-Lysine (PLL)-coated dishes or by confining the cells in 25 µm microchannels (Channels; n=41, 7, 8 individual measurements from 1-3 independent experiments; p=0.11, 0.98). (d) Cortex thickness measurements for HeLa cells blocked in prometaphase with S-Trityl-L-cysteine (STC-Blocked) and unblocked mitotic HeLa cells identified based on morphology and chromosome appearance (n=100, 16 individual measurements from 13 (STC-blocked) and 1 (unblocked) independent experiments; p=0.2565). (e) Left: calculation of average cortical actin density using the cortical thickness extraction method (Ref. 24 in the main text). Right: calculation of total cortical actin amount using the measured cell radius (r) and cortex thickness (h). (f,g) Relative cortex density (p=1.2×10^{-6}, 0.018, 0.032, 0.0023) (f) and amount (p=0.47, 0.66, 0.40, 0.53) (g) for different cell lines in interphase and mitosis. Values were normalized by dividing by the median of the interphase value for each cell line (n=41, 100, 47, 27, 11, 13, 22, 13 individual cell measurements from 2-13 independent experiments). (h) Example segmentation mask (bottom) applied to a scanning electron micrograph of membrane-extracted cortices (top, from Fig. 1g). Images are representative of 17 regions from 8 cells (2 independent experiments). Scale bars = 100 nm. (i) Frequency distribution of pore sizes for adherent Hela and S-HeLa cells in interphase and mitosis (n=14, 19, 18, 17 regions from 9, 13, 8, 8 cells from 2 independent experiments). Size distributions were comparable between interphase and mitosis, with slightly more large pores in interphase compared to metaphase (inset). (j) Pore coverage (%) in HeLa and S-HeLa cells in interphase and mitosis from regions analysed in (*i*)

$(p=4.3 \times 10^{-6}, 0.59)$. The average pore coverage was unchanged in S-HeLa cells and slightly higher in mitosis in HeLa cells. However, SEM only probes the outer surface of the cortex; it is thus difficult to draw conclusions about overall cortical actin density from this analysis. For all panels, Welch's t-test p-values: $^{ns}p>0.05$, $*p<0.05$, $**p<0.01$, $***p<0.001$.

Supplementary Figure 3: Extended measurements of cortex properties upon depletion of cortex thickness regulators. (a) Cortex thickness measurements for mitotic HeLa cells treated with the myosin-II inhibitor Blebbistatin (Blebb.), the Arp2/3 inhibitor CK-666 and corresponding DMSO controls (n=12, 16, 27, 33 individual measurements from 2-3 independent experiments; p=0.078, 0.47). (b) Cortex tension measurements following treatment with the actin stabilizing drug Jasplakinolide (Jas.), Blebbistatin (Blebb.) and corresponding DMSO controls (n=13, 16, 21, 38 individual measurements from 3 independent experiments; $p=8.1 \times 10^{-5}$, 3.4×10^{-7}). (c,d) Boxplot comparing the full width at half maximum (FWHM) of the membrane linescan (p=0.94, 0.20, 0.0065) (c) and cell radii (p=0.19, 0.084, 0.31) (d) in mitotic HeLa cells following siRNA against *CAPZB*, *CFL1* and *DIAPH1* (n=38, 17, 40, 44, 20, 20 individual measurements from 3-4 independent experiments). The membrane FWHM was ~10-15% smaller in *DIAPH1* knockdown cells, not enough to account for the ~60% reduction in cortex thickness. (e) Scatter plot of cortex thickness vs. cell radius for all measured conditions in mitotic HeLa cells (untreated, target knockdowns and corresponding scrambled controls [Scr.]). (f,g) Relative cortex density (p=0.23, 0.0008, 0.059) (f) and amount ($p=1.4 \times 10^{-5}$, 3.6×10^{-7}, 0.016) (g) in mitotic HeLa cells treated with siRNA against *CAPZB*, *CFL1* and *DIAPH1* (Target) and corresponding scrambled controls (Scr.). Values were normalized by dividing by

3

the median of the corresponding Scr. control (n=38, 17, 40, 44, 20, 20 individual measurements from 3-4 independent experiments). Cortex density and amount were calculated as described in Supplementary Fig. 2e. (h) Western blot showing the levels of active myosin light chain (pMLC2-Ser19) and total myosin light chain (MLC2) in whole cell lysates of mitotic HeLa cells treated with siRNA against *CAPZB*, *DIAPH1*, or *CFL1*, and corresponding scrambled (Scr.) controls. GAPDH, β-Actin and α-Tubulin were used as loading controls. Blots are representative of at least 3 independent experiments. Uncropped Western blots are provided in Supplementary Fig. 7. (i) Quantification of the Western blot shown in panel h, showing the mitotic levels of MLC2 and pMLC2-Ser19 in each knockdown relative to its Scr. siRNA control. For all panels, Welch's t-test p-values: $^{ns}p>0.05$, $*p<0.05$, $**p<0.01$, $***p<0.001$.

Supplementary Figure 4: Depletion efficiency for the targeted siRNA screen for cortex thickness regulators. The bar plot shows the mRNA expression levels (RQ) in adherent HeLa cells treated with siRNA against various ABPs normalized to mRNA levels in control non-silencing pools (RQ (Norm.)). RQ levels were calculated by normalizing mRNA levels of queried genes to the averaged levels of GAPDH and ACTB. Relative mRNA abundance (RQ (Norm.)) was then calculated by dividing by the RQ value for control pools. Differences were considered significant if RQ (Norm.) was reduced by at least 40%. qPCR analysis was performed once for all siRNA conditions. For hits from the targeted ABP screen, Western blots were performed (Fig. 3b).

Supplementary Figure 5: Computer simulations of tension generation in a

crosslinked actomyosin cortex. (a) Actin filament representation (left): **r** is the centre of mass, s describes a position along the filament and the unit vector **n** is oriented towards the plus end of the filament. Myosin minifilament representation (right) with the centre of mass (**r**), orientation vector (**n**) and the two connecting heads. (b) Initialized network with a seeding thickness h_0 and width W. Grayed filaments cross periodic boundaries in the x and y directions. (c) Myosin head attachment (top) and force balance on the myosin-actin attachment point (bottom). v_s is the velocity of the myosin, α_s is a friction coefficient, f_0 is the myosin stall force and $\boldsymbol{f_{ms}}$ is the spring force of the myosin head. (d) Schematic of actin filament i with three springs connected, force balance on the filament, and sliced filament for surface tension measurement. The resulting force $f\perp_i$ along the normal of the slicing plane is used for calculating the total force. (e) Tension as a function of mean filament length for simulations where filament lengths were chosen according to a Gaussian distribution around a mean length. The standard deviations of the Gaussian distribution were 10% (blue), 20% (red), and 30% (green) of the mean length. (f) Tension as a function of the seeding thickness at constant filament length, density and number of motors. Seeding thickness is varied by changing the number of filaments. (g) Tension as a function of filament length at constant seeding thickness and density. The total number of filaments is adjusted to keep the total amount (length) of actin, $L_a = N_f l_a$, constant. For (e-g), each point represents the mean of 9 simulations, ±SD. Tensions are normalized to $T_0 = 230$ pN/μm.

Supplementary Figure 6: Effect of mitotic thickness regulators on the interphase cortex. Boxplots comparing (a) cortex thickness (p=0.0016, 0.79, 0.16), (b) cortex tension (p=0.018, 0.0025, 0.48), (c) relative cortex density (p=0.0002, 6.3x10^{-5},

0.031), and (d) relative actin amount ($p=1.5 \times 10^{-7}$, 0.023, 0.014) between interphase HeLa cells treated with siRNA targeted against *CAPZB*, *CFL1* or *DIAPH1* (Target, blue) or the corresponding scrambled siRNAs (Scr., black). Relative values were normalized to the median of the corresponding Scr. control. Points represent individual measurements (n=33, 33, 31, 36, 26, 20 cells from 3 independent experiments for thickness, density and amount measurements; n=22, 37, 20, 24, 23, 36 cells from 3-4 independent experiments for cortex tension measurements). Cortex thickness increased upon depletion of CAPZB, but did not significantly change upon *CFL1* and *DIAPH1* knockdown. Cortex tension increased upon depletion of CAPZB and CFL1 (as previously reported for CFL1, Ref [13]), but did not significantly change upon DIAPH1 depletion. These results could suggest a mitosis-specific role of DIAPH1 in thickness/tension regulation. (e) Western blots showing the levels of CAPZB, CFL1, and DIAPH1 in whole cell lysates of interphase (Thymidine-blocked) and mitotic (STLC-blocked) HeLa cells. GAPDH was used as a loading control. Blots are representative from 7 independent experiments. (f) Boxplots comparing the interphase/mitosis ratio of normalized CAPZB, CFL1, and DIAPH1 expression from 7 independent experiments. The whole cell levels of both CAPZB and CFL1 were higher in interphase than in mitosis, while DIAPH1 levels did not change. This suggests that the hits identified in our screen do not directly control the cortical thinning between interphase and mitosis. However, it is important to note that Western blot analysis reflects whole cell levels and may not reflect changes in cortical localization. Furthermore, these experiments do not take into account any possible post-translational modification of these proteins. Dotted line (ratio = 1) signifies no change in levels between interphase and mitosis. Uncropped western blots are provided in Supplementary Fig. 7. Welch's t-test p-values: [ns]$p>0.05$, *$p<0.05$,

**p<0.01, ***p<0.001.

Supplementary Figure 7: Uncropped Western blots for Fig. 3b, Supplementary Fig. 3h and Supplementary Figure 6e. Red dotted lines indicate regions that were cropped for the figures.

Supplementary Tables:

Supplementary Table 1: Thickness and volume changes between interphase and mitosis. Expected changes in mitotic cortical thickness ($h_{expected,m}$) assuming conserved cortex volume was calculated from the median radius in interphase (r_i), median radius in mitosis (r_m) and median cortex thickness in interphase (h_i) using the formula, $h_{expected,m} \approx (r_i^2 * h_i)/r_m^2$, and compared to the measured mitotic cortex thickness (h_m).

Supplementary Table 2: Detailed information about siRNA knockdown conditions in Fig. 2. The table includes supplementary references 16-18 (see Supplementary Note). Each ABP was depleted using siRNA previously shown to reduce expression, or siRNA pools.

Supplementary Table 3: Primers used for qPCR to test siRNA knockdown efficiency in Supplementary Fig. 4.

Supplementary Table 4: Median cortex stress. Median cortical stress was calculated from the ratio of median tension and median thickness for all conditions.

Supplementary Table 5: Simulation Parameters. Whenever possible, simulation parameters were estimated from literature or chosen so that the appearance of the simulated cortex is comparable to experimental observations. The table includes supplementary references 1 and 5 (see Supplementary Note).

Supplementary Videos:

Supplementary Video 1: Simulation of a 3D cortex with 200 nm long actin filaments. *Left*: xy and xz views of the simulated cortex with l_a = 200 nm. *Right*: Evolution of tension over time during the simulation run.
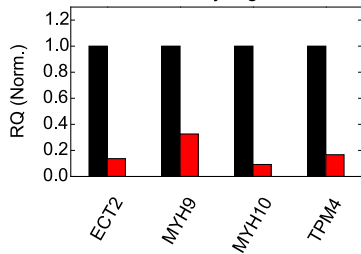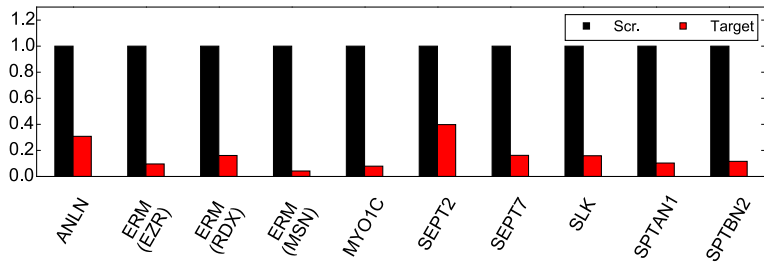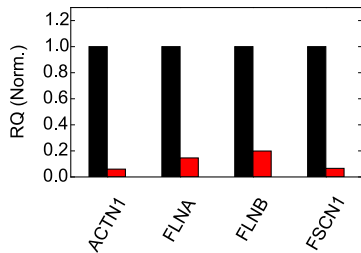

Supplementary Video 2: Simulation of a 3D cortex with 500 nm long actin filaments. *Left*: xy and xz views of the simulated cortex with la = 500 nm. *Right*: Evolution of tension over time during the simulation run.

Supplementary Video 3: Simulation of a 3D cortex with 740 nm long actin filaments. *Left*: xy and xz views of the simulated cortex with la = 740 nm. *Right*: Evolution of tension over time during the simulation run.

a

b h_{cell}, r_c, r_{mid}

c Force, F [nN] — Time [s]

d

- mES cell (n = 30)
- Linear fitting

Cell height by AFM [μm]

Cell height by membrane
peak-to-peak distance [μm]

In panel **e**:

$$\text{Density} = \frac{i_c - i_{\text{in}}}{\langle i_{\text{actin}[x_0, x_{\text{out}}]} \rangle}$$

$$V = \frac{4}{3}\pi(r^3 - (r-h)^3)$$

$$\text{Actin Amount} = \text{Density} \cdot V$$
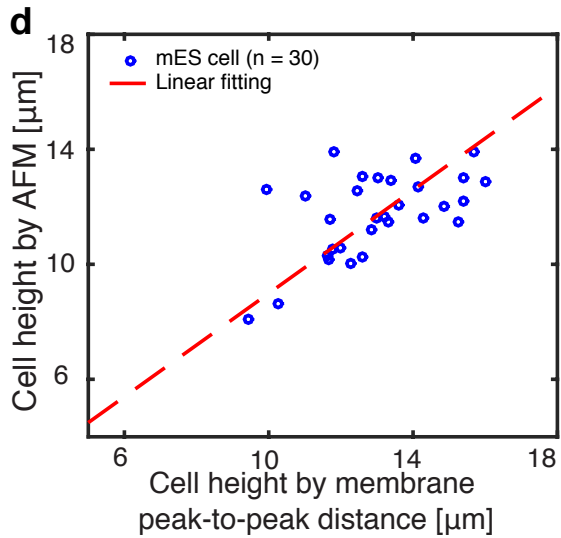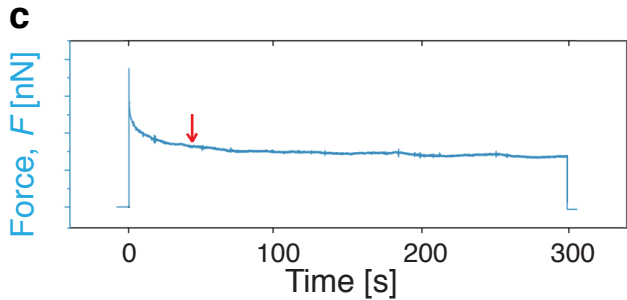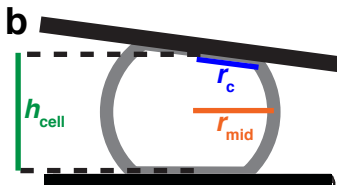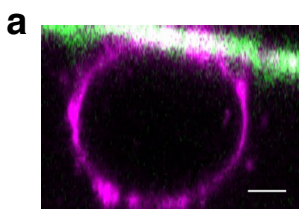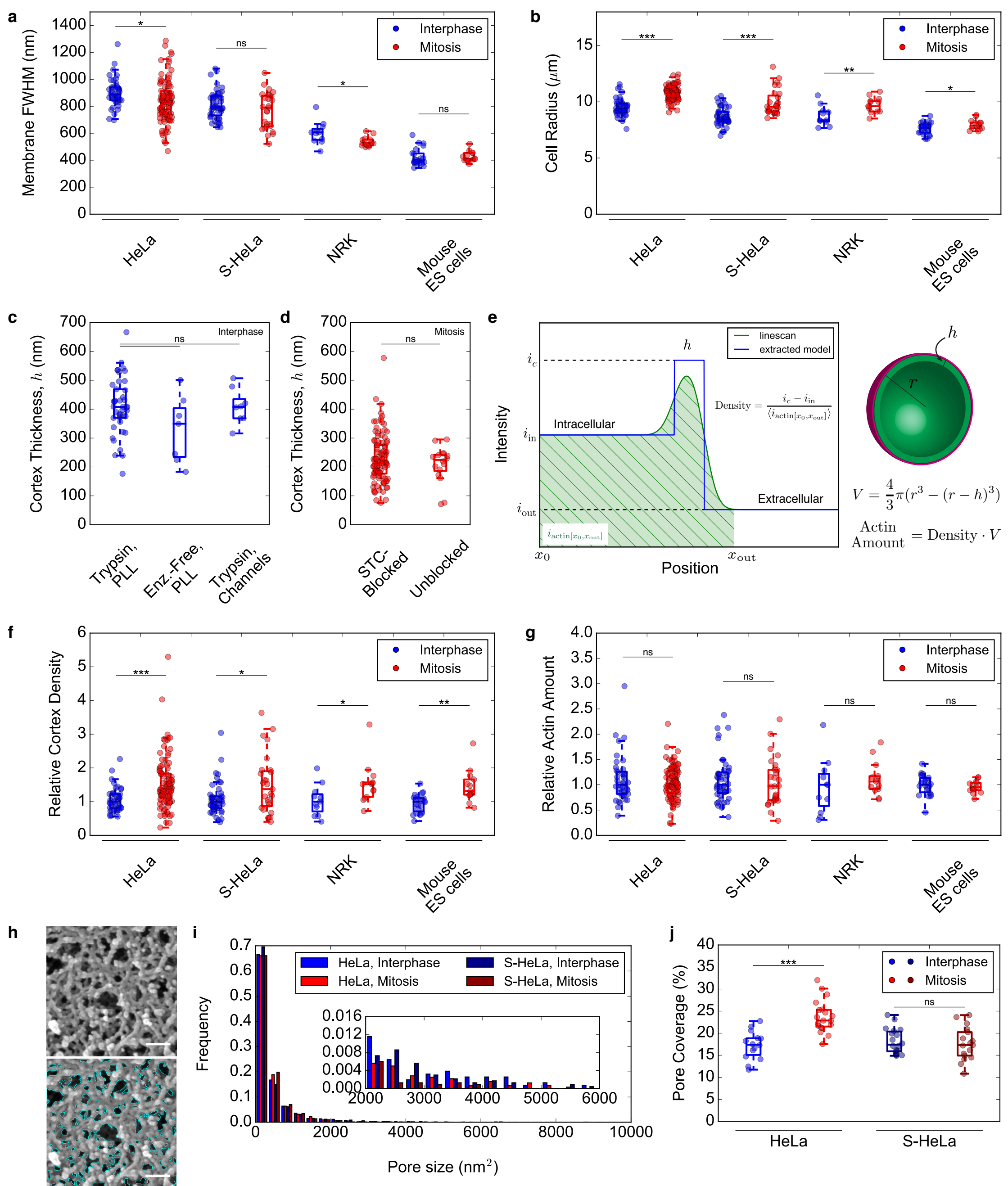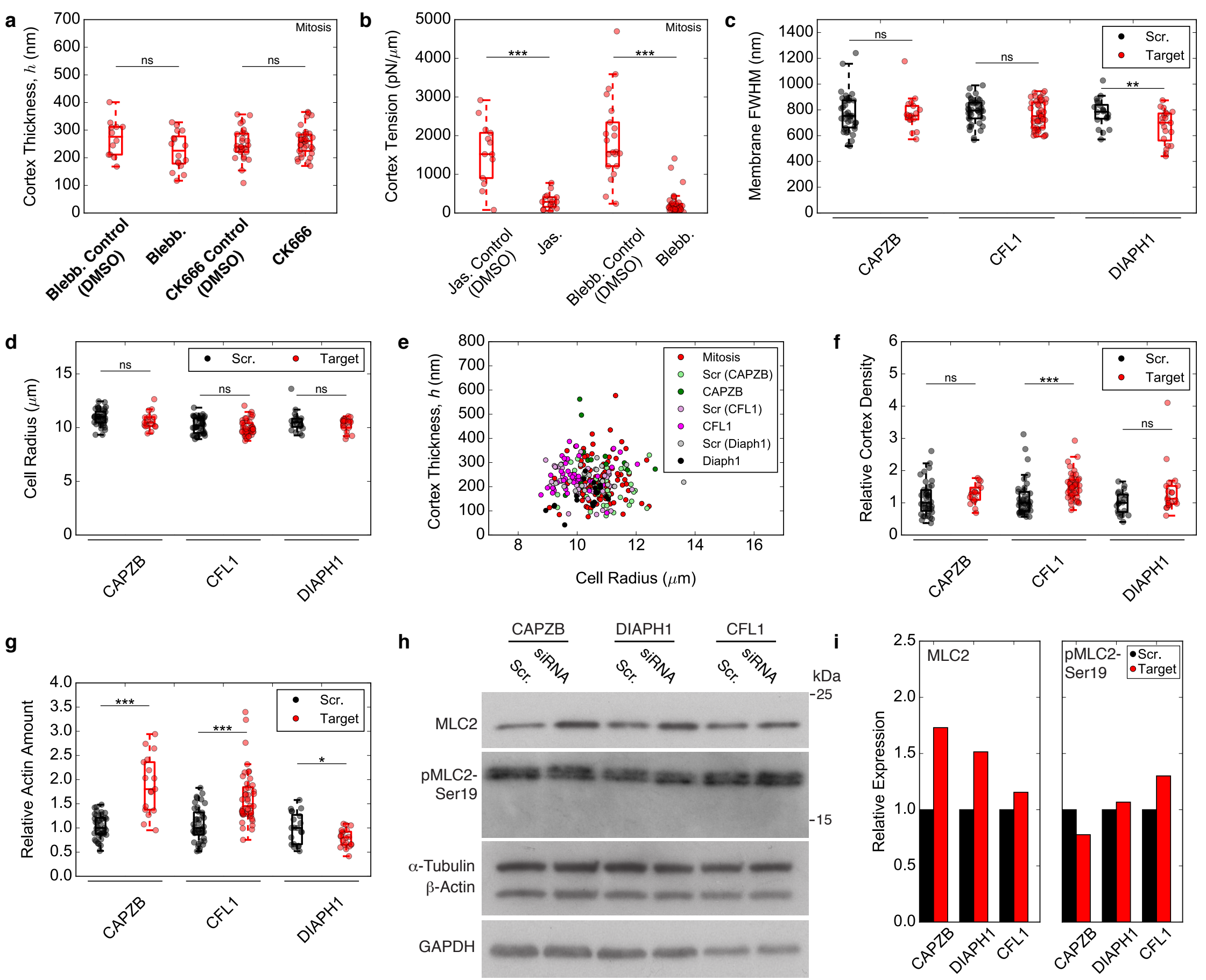
a Contractility regulators

b Cortex-membrane linkers

c Crosslinkers

d Actin filament length regulators

Legend: ■ Scr. ■ Target

a actin   myosin

b W h_0

c s_{ki} $\mathbf{f}_{ms}$ $-\alpha_s \mathbf{y}_s$ f_0

d $\mathbf{f}_{1i}$ s_{1i} s_{2i} s_{3i} $\mathbf{f}_{2i}$ $\mathbf{f}_{3i}$ $\mathbf{f}_{\perp i}$

e Tension (T/T_0) Length (nm)   10%   20%   30%

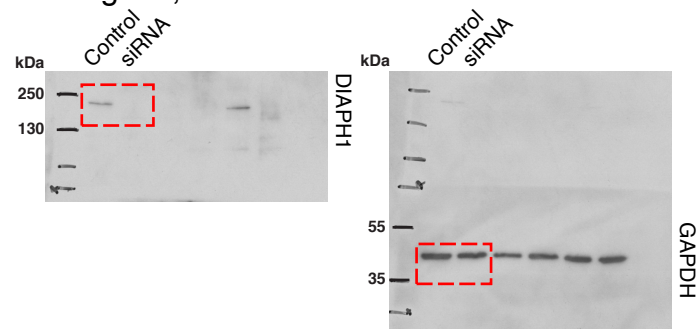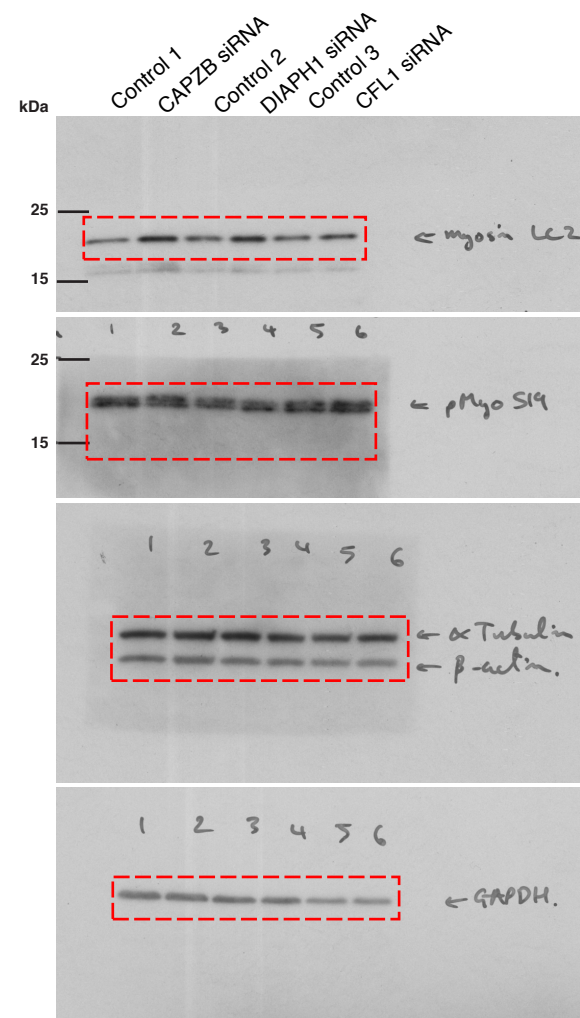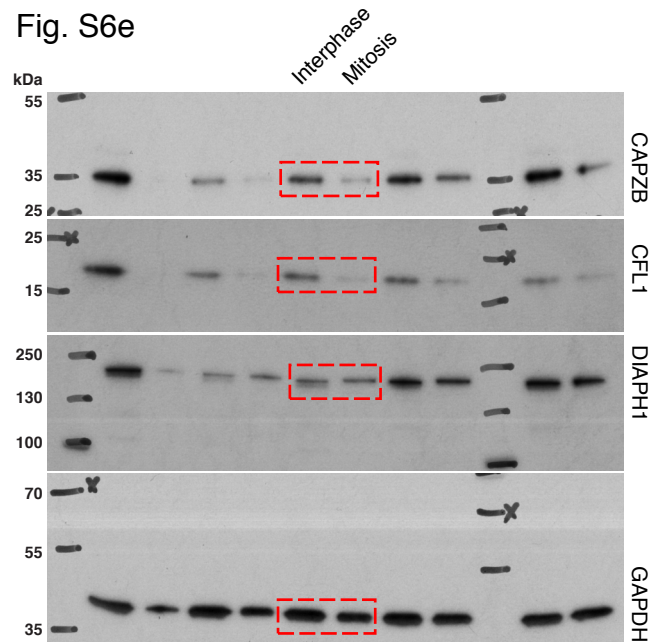**f** Tension (T/T_0) Thickness (nm)

g Tension (T/T_0) Length (nm)
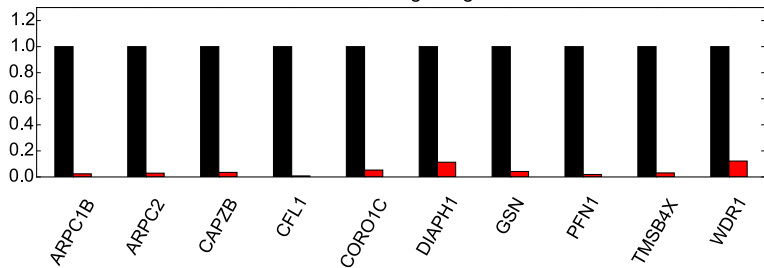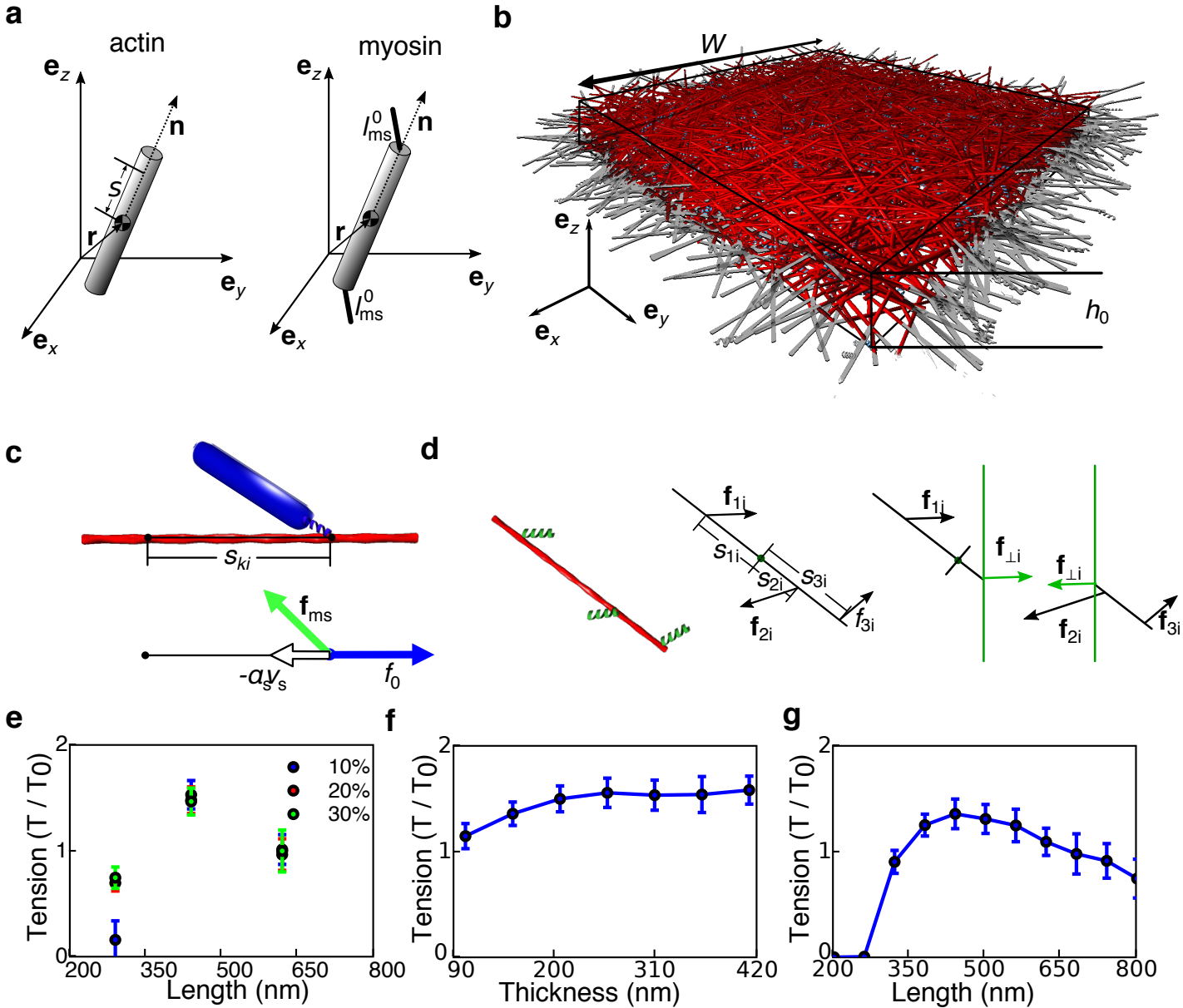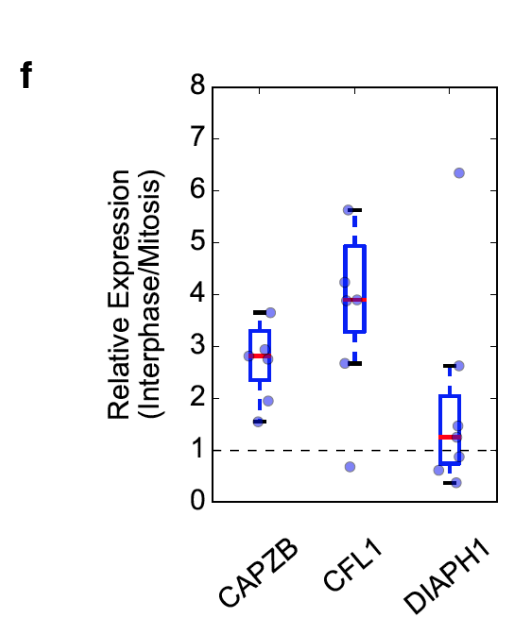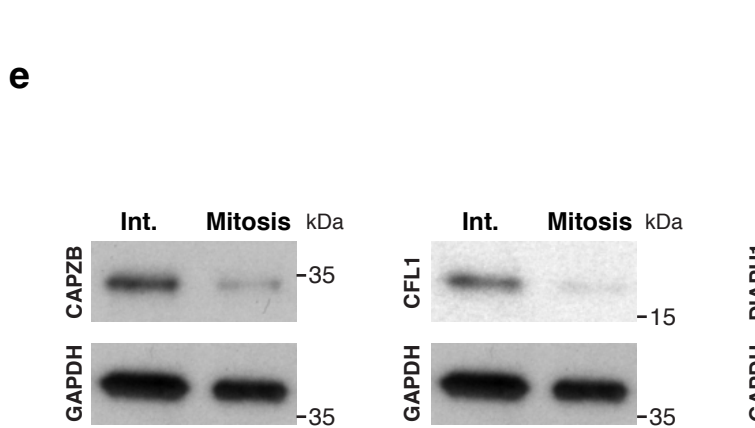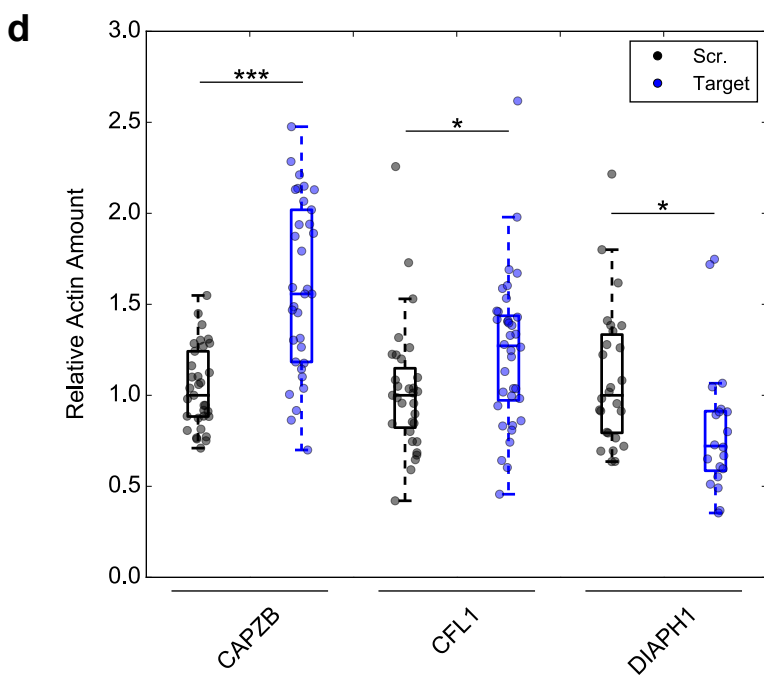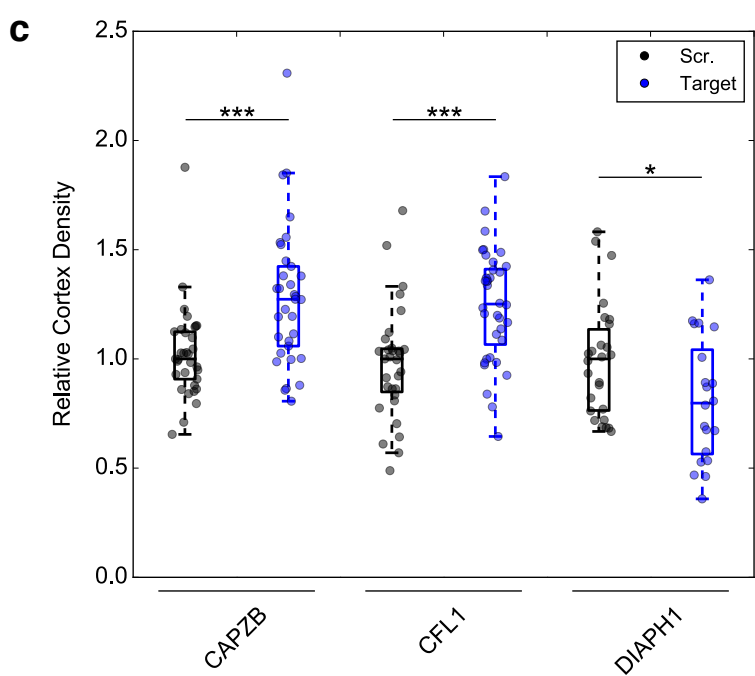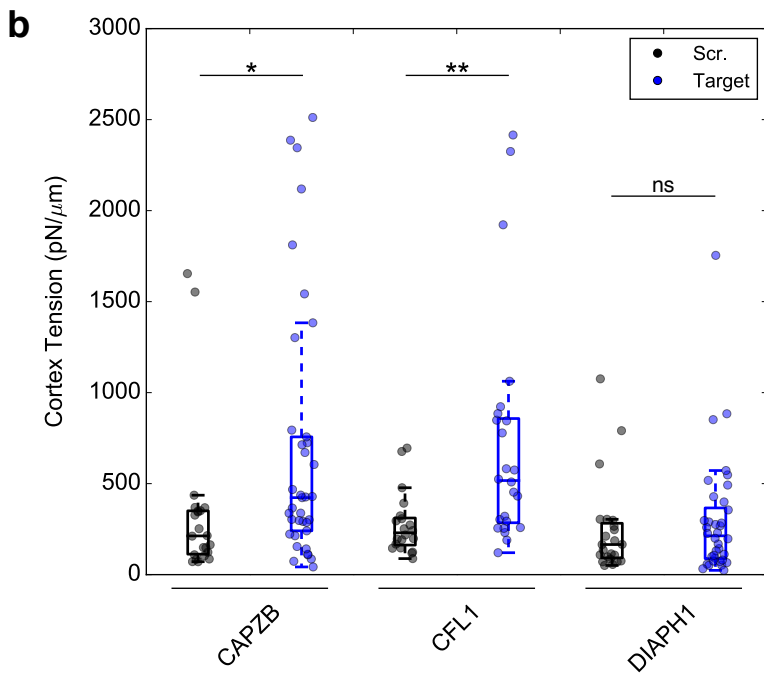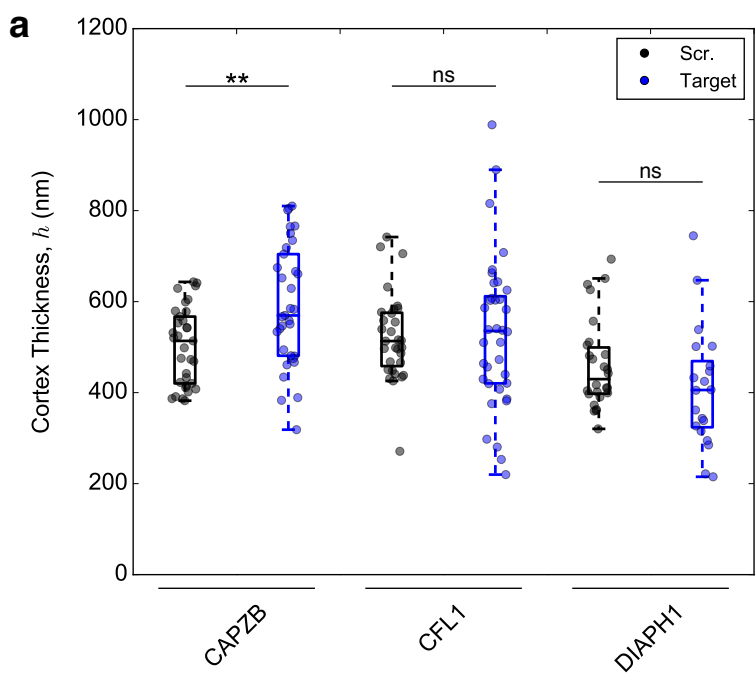
a Fig. 3b, top
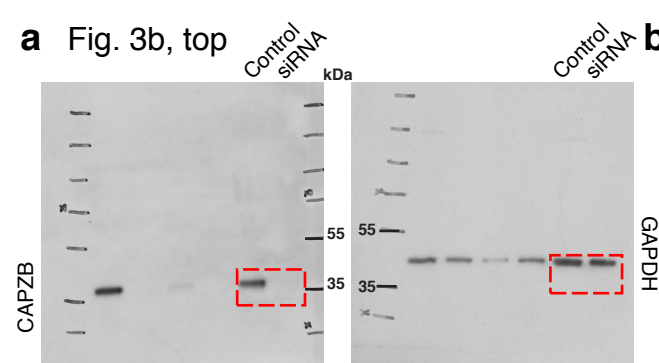
b Fig. 3b, centre
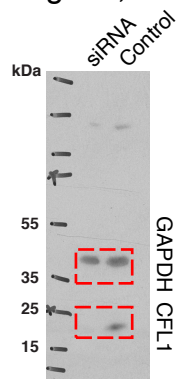
c Fig. 3b, bottom

d Fig. S3h

e Fig. S6e

Table 1

Cell type	Interphase Radius (μm) (r_i)	Mitotic Radius (μm) (r_m)	Interphase Thickness (μm) (h_i)	Expected Mitotic Thickness (μm) $(h_{expected,m})$	Observed Mitotic Thickness (μm) (h_m)
HeLa	9.4	10.75	0.408	0.312	0.215
S-HeLa	8.49	9.57	0.312	0.245	0.169
NRK	8.35	9.61	0.249	0.188	0.167
mESCs	7.67	7.87	0.168	0.16	0.095

Table 3

Gene symbol	Forward primer	Reverse primer
ECT2	ctctaggtgagcacccctgt	tgtgccgttttcttgctatct
MYH9	tgaggcagaagcactcacag	ctttgccttctcgaggtttg
MYH10	ggaggacacgctggacac	tctgccacttcttgttcacg
TPM4	cgcaaatacgaggaggtagc	tcttcttccaggtcaccaca
ANLN	gggctgaactcaagattgga	ctgcaagtttttgcatacgtg
EZR	ttgcagaatacactgccaaga	aggtcatcctgggcttcttt
RDX	gagctgctgaagaggcaaag	ttggcagtgaattcagcaag
MSN	tcaagaacaagaaaggctcaga	gcctatcttgggagttagtctgtc
MYO1C	ctcatcaccaaggccaaga	cctttatcaccgagaattcagc
SEPT2	aaggcaatacacaacaaggtga	ttcttcaatttcatccagaatcc
SEPT7	gaagttaatggcaaaagggtca	tcaagtcctgcatgtgtgttc
SLK	gagtggagagagaaattgagaccta	cttcctgttcctgtagtttcctg
SPTAN1	atacctcctcgatgggtcct	ggatttcctggtgcttgc
SPTBN2	gcctacgagcatgacattcag	gccttgtctccagcgtagg
ACTN1	atgcagccagaagaggactg	ttacaccatgccgtgaatgt
FLNA	gtcagcatccccaacagc	actccggggccgtatactt
FLNB	gaggaggcaccggtaaatg	gtcactcactgggacataggc
FSCN1	gccaacgagaggaacgtg	ggcacacttttggtgtcg
ARPC1B	ggcgctgaccttcatcac	gcgtcataggtgaacagcac
ARPC2	gccccacaggtcctcttta	tgacgagggaacagcaca
CAPZB	tggaaaaacaaaggatatcgtca	gcttcttgttttgatttgtctgc
CFL1	gtgccctctccttttcgttt	ttgaacaccttgatgacaccat
CORO1C	ttgccataatcatagaggcaag	gatttgtcaattcgaccagtctt
DIAPH1	gaggccaaactggtccaa	ttgttctcaaagcggtcctc
GSN	tctgccatcctgactgctc	cttggaccacacggctct
PFN1	ccttcaatgtcactgtcacca	accaccgtggacaccttct
TMSB4X	cgaaactgaagaagacagagacg	ttgcttctcctgttcaatcgt
WDR1	agaaacaaccccagcaagc	cgtggctcccagagtaaatg
ACTB	attggcaatgagcggttc	tgaaggtagtttcgtggatgc
GAPDH	agccacatcgctcagacac	gcccaatacgaccaaatcc

Table 4

Condition	Median tension (pN/μm)	Median thickness (μm)	Stress (Pa)
Interphase Untreated	159	0.408	389
Mitosis Untreated	1172	0.215	5456
Mitosis CAPZB Scr.	891	0.186	4800
Mitosis CAPZB siRNA	468	0.294	1594
Mitosis CFL1 Scr.	999	0.213	4682
Mitosis CFL1 siRNA	529	0.231	2290
Mitosis DIAPH1 Scr.	1230	0.223	5517
Mitosis DIAPH1 siRNA	358	0.16	2231